

AN X-RAY SPECTROSCOPIC STUDY OF THE SMC X-1/Sk 160 SYSTEM

PATRICK S. WOJDOWSKI¹ AND GEORGE W. CLARK

Physics Department and Center for Space Research, Massachusetts Institute of Technology, Cambridge, MA 02139

AND

TIMOTHY R. KALLMAN

NASA/Goddard Space Flight Center, Greenbelt, MD 20771

Received 1999 September 30; accepted 2000 June 8

ABSTRACT

We have investigated the composition and distribution of the wind of Sk 160, the supergiant companion of the X-ray star SMC X-1, by comparing an X-ray spectrum of the source, obtained with the *ASCA* observatory, during an eclipse with the computed spectra of reprocessed radiation from circumstellar matter with various density distributions. We show that the metal abundance in the wind of Sk 160 is no greater than a few tenths of solar, as has been determined for other objects in the Magellanic Clouds. We also show that the observed X-ray spectrum is not consistent with the density distributions of circumstellar matter of the spherically symmetric form derived for line-driven winds, nor with the density distribution derived from a hydrodynamic simulation of the X-ray perturbed and line-driven wind by Blondin & Woo.

Subject headings: pulsars: individual (SMC X-1) — stars: winds, outflows — techniques: spectroscopic — X-rays: binaries

1. INTRODUCTION

The evidence that some of the first discovered cosmic X-ray sources were binary star systems included periodic “low-states” that were recognized as eclipses by a companion star. However, it was observed that during these eclipses there was still a residual flux of X-rays. Schreier et al. (1972) observed a residual flux from Cen X-3 during its eclipses and proposed that it might be due to “the slow radiative cooling of the gas surrounding the system which is heated by the pulsating source.” In observations with the GSFC Cosmic X-ray Spectroscopy experiment on board *OSO-8*, Becker et al. (1978) detected a significant flux of residual X-rays during three eclipses of the massive X-ray binary Vela X-1 and argued—on the grounds that the residual eclipse X-ray had, within limits, the same spectrum as the unclipped flux—that this eclipse radiation was most likely due to X-ray scattering around the primary star.

Observations of the P-Cygni profiles of ultraviolet lines in massive stars showed that strong winds are a ubiquitous feature of massive stars Morton (1967). These winds are driven as the UV radiation from the star transfers its outward momentum to the wind in line transitions (Lucy & Solomon 1970; Castor, Abbott, & Klein 1975). In high-mass X-ray binaries (HMXBs) then, an obvious source of circumstellar material exists to scatter or reprocess the X-rays from the compact object and allow X-rays from these sources to be observed during eclipse.

Information on the composition and dynamics of HMXB winds may provide important clues for the understanding of binary evolution (e.g., mass-loss rates). Information on the metal abundances may also inform the study of binary evolution. In other galaxies, such as the Magellanic Clouds, X-ray reprocessing in the winds of HMXB may provide another way to measure the metal abundances in those

galaxies and therefore inform the study of the evolution of those galaxies.

Properties of HMXB winds have been inferred in studies that interpret the X-ray spectrum at various phases in terms of the absorption, emission, and scattering by the wind material. Studies of X-ray absorption during eclipse transitions have shown that the atmospheric densities near the surfaces of the massive companions decrease exponentially atmospheres with scale heights $\sim 1/10$ of the stellar radius (Schreier et al. 1972; Sato et al. 1986; Clark, Minato, & Mi 1988). Such exponential regions are not predicted by the theory of Castor et al. (1975) or subsequent refinements (e.g., Pauldrach, Puls, & Kudritzki 1986; Kudritzki et al. 1989), which assume that the wind is spherically symmetric. X-rays photoionize the wind, destroying the ions responsible for the radiation driving, and shutting off the wind acceleration, in the region illuminated by the X-ray star. Hydrodynamic simulations have been done to explore the behavior of winds in HMXB under the influence of X-ray ionization and of X-ray heating of the exposed face of the companion star (Blondin et al. 1990; Blondin 1994; Blondin & Woo 1995).

Several studies have compared observations with the results of Monte Carlo calculations with model winds. In these calculations, individual photons were tracked through trial wind density distributions where they could scatter from electrons or be absorbed. Fluorescent photons were emitted following inner shell ionization, and these photons were tracked through the wind in the same way. Lewis et al. (1992) found that *Ginga* spectra of Vela X-1 could be reproduced with a density distribution of the form of a radiatively driven wind with an exponential lower region. Clark, Woo, & Nagase (1994) attempted to reproduce *Ginga* spectra of 4U 1538–52 with a similar density distribution but with added components resembling structures in the simulations of Blondin et al. (1990). These authors were able to reproduce the observed spectrum above 4.5 keV. They attributed an excess at lower energies in part to a dust-scattered halo.

¹ Current Address: Lawrence Livermore National Laboratory, P. O. Box 808, L-41, Livermore, CA 94551, patrickw@virgo.llnl.gov.

Woo et al. (1995) found that *Ginga* spectra of SMC X-1 could be reproduced from the calculated density distribution of Blondin & Woo (1995).

Spectra from the moderate-resolution ($E/\Delta E \sim 15$ at 1 keV) X-ray CCDs on *ASCA*—and the prospect of high resolution X-ray spectra from *AXAF*, *XMM*, and *ASTRO-E*—present new opportunities for using X-ray spectra in the study of HMXB winds. In an observation of Vela X-1 with *ASCA*, approximately 10 emission features emerged in the spectrum of the system viewed during eclipse of the X-ray source when the much more intense, featureless continuum radiation was occulted. Most of these emission features were identified as $K\alpha$ emission lines from helium and hydrogen-like ions of astrophysically abundant metals (Nagase et al. 1994). The Monte Carlo spectral calculations described above did not include recombination to highly ionized atoms, which is responsible for these lines, and so could not have predicted this spectrum. Moderate- and high-resolution spectra provide a powerful diagnostic of the conditions in the wind through study of this recombination radiation.

Ebisawa et al. (1996) have estimated the size of the ionized regions in the wind in the Cen X-3 system from the magnitude of the recombination lines measured with *ASCA* and Liedahl & Paerels (1996) have estimated the emission measure of ionized regions in the wind of the Cyg X-3 system from the recombination lines and narrow recombination continua in the *ASCA* spectrum. Sako et al. (1999) have estimated the differential emission measure of the wind of Vela X-1 from the recombination features. They also developed a method to compute the emission spectrum of recombination from a given matter distribution and have inferred the presence of additional dense matter in the Vela X-1 wind from the presence of fluorescence lines.

In this paper, we present a study of the circumstellar matter in the SMC X-1/Sk 160 binary system based on observations of SMC X-1 in and out of eclipse. Using the XSTAR program, we calculate the spectra of reprocessed radiation for a range of values of the ionization parameter ($\xi \equiv L/nr^2$). We show that the eclipse spectrum of SMC X-1, which is similar in shape to the out-of-eclipse spectrum, resembles the spectra of X-rays reprocessed in material with either low or high ionization parameters but not the spectra expected from material with intermediate ionization parameters, which should exhibit strong recombination features. We then describe a method to calculate the spectra of reprocessed X-rays from an arbitrary wind distribution. This method takes account of electron scattering and fluorescence and calculates the reprocessed emission by summing the diffuse emission and absorbing along the lines of sight to the observer. We use this method to predict the spectrum of X-rays emitted by a wind with the density distribution of Blondin & Woo (1995). Because our calculations include recombination radiation and because the *ASCA* data is sensitive to recombination spectral features, we obtain a conclusion which contradicts that of Woo et al. (1995). The matter distribution of Blondin & Woo (1995) would produce strong recombination radiation features, which are excluded by the observed *ASCA* eclipse spectrum.

In § 2 we discuss our observations of SMC X-1 with *ASCA*. In § 3 we discuss our calculations of the spectra of reprocessed X-rays from homogenous, optically thin gas, and compare it to the *ASCA* data. In § 4 we describe our procedure for computing the spectrum of reprocessing from

a three-dimensional distribution of gas and apply it to the density distribution from the hydrodynamic simulation by Blondin & Woo (1995).

2. *ASCA* OBSERVATIONS

SMC X-1 has been observed twice by the *ASCA* observatory: once, while the source was uneclipsed, soon after launch in 1993 April during the performance verification (PV) phase, and again in 1995 October, while the source was eclipsed. The out-of-eclipse observation, yielded 17,769 s of SIS0 data and 17,573 s of SIS1 data after screening according to the default criteria described in the *ASCA* Data Reduction Guide. During the eclipsed observation, SMC X-1 was observed over a period of approximately 94,000 s resulting in 32,838 s of SIS0 data and 32,239 s of SIS1 data after screening.

We used the FTOOLS package to extract light curves and spectra from these data and the XSPEC (Arnaud 1996) program to do the spectral analysis. The source regions of the CCD chips were chosen to be squares centered on the image of SMC X-1 and $383''$ on a side. The remainders of the chips were used as the background regions. To derive spectra and light curves, the number of counts in each spectral or time bin in the background region was subtracted (after correcting for the difference in the relative sizes of the source and background regions) from the counts in the corresponding source bin.

Light curves for both observations are plotted in Figure 1 along with a light curve from *Ginga* from an observation described by Woo et al. (1995) in the energy band where that instrument's energy band overlaps *ASCA*'s. The *Ginga* light curve illustrates the "high state" behavior of SMC X-1 with sharp eclipse transitions at phases ± 0.07 . A spectrum was extracted from the out-of-eclipse *ASCA* observation using all but a few hundred seconds at the end where the count rate started to decrease, possibly due to an onset of the low state (not visible in Fig. 1). The resulting exposures were 17,226 s for SIS0 and 17,026 s for SIS1. Spectra were extracted from the entire time of the eclipse observation though that observation extends beyond the time of nominal eclipse. The fact that the flux from SMC X-1 differed by no more than a factor of 3 between times inside and outside of the nominal eclipses indicates that the system was in the low-state—with the compact object blocked by the precessing accretion disk (Wojdowski et al. 1998). Since the X-rays detected during that observation have been reprocessed in the stellar wind, all of the data from that observation, including that from outside of the nominal eclipse, were used in our analysis in order to improve the signal-to-noise ratio of the eclipse spectrum. To further improve the signal the energy channels, which oversample the detector resolution, were grouped so that each channel has at least 50 counts.

Because of the high count rate in the out-of-eclipse observation, the errors due to counting statistics were small compared to the systematic errors due to the instrument calibration and the data from the two detectors could not simultaneously be fitted to a single trial spectrum. For this reason, only the data from the SIS0 detector, which may be better calibrated, were used in spectral fits for this observation. The spectrum derived from the out-of-eclipse observation was well fitted by a model that consists of a power-law plus two broad gaussian components (one near 0.9 keV and one near 6 keV) absorbed by a small column of

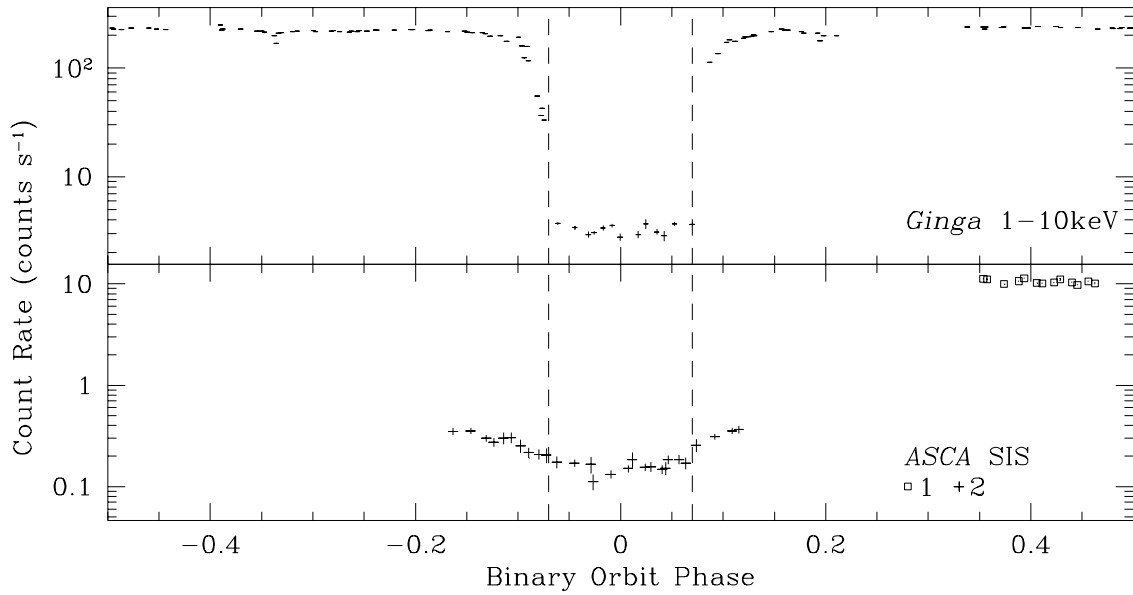


FIG. 1.—Count rate of SMC X-1 as a function of orbital phase in the two observations (1 refers to the 1993 observation and 2 to the 1995 observation) with the *ASCA* SIS (count rate is the sum of the two detectors) and in an observation with *Ginga* (count rate is in the 1-10 keV band only).

cold interstellar material. The fitted model for the photon flux is

$$\mathcal{F}(E) = e^{-\sigma(E)N_H} [f_{pl}(E) + f_{ga1}(E) + f_{ga2}(E)]$$

$$\times \begin{cases} 1, & E \leq 10 \text{ keV}, \\ \exp\left(-\frac{E - 10 \text{ keV}}{15 \text{ keV}}\right), & E > 10 \text{ keV}, \end{cases} \quad (1)$$

where

$$f_{pl}(E) = K_{pl}(E/1 \text{ keV})^{-\alpha}, \quad (2)$$

$$f_{gai}(E) = \frac{K_{gai}}{\sigma_i \sqrt{2\pi}} \exp\left(-\frac{(E - E_i)^2}{2\sigma_i^2}\right), \quad (3)$$

and $\sigma(E)$ is the cross section of interstellar absorption of Morrison & McCammon (1983). While the sensitivity of the *ASCA* detectors does not extend to the high energy cut-off, it has been measured with *Ginga* (Woo et al. 1995) and is

included here for consistency with the XSTAR calculations. The observed spectra and best-fit model are plotted in Figure 2. Though they were not used in the spectral fits, the data from the SIS1 detector are included in this plot. There is a discrepancy between the two detectors near 1.3 keV that is comparable to the channel-to-channel variations in observations of the supernova remnant 3C 273 (Orr et al. 1998) that were used for calibration. The best-fit values of the parameters for this and the two fits described below are tabulated in Table 1. Approximately the same result was obtained by Stahle et al. (1997) for this data set. The fitted value for the column of neutral hydrogen lies between values estimated by interpolation from neighboring directions in 21-cm emission surveys: $4.6 \times 10^{20} \text{ cm}^{-2}$ for a galactic survey with 1° resolution (Dickey & Lockman 1990) and $4.5 \times 10^{21} \text{ cm}^{-2}$ for a survey of the SMC with $98''$ resolution (Stanimirovic et al. 1999). The flux of this model spectrum in the 13.6 eV–13.6 keV band (the band in which luminosity is defined in XSTAR) is $6.44 \times 10^{-10} \text{ ergs cm}^{-2} \text{ s}^{-1}$. For isotropic emission, this corresponds to a

TABLE 1
BEST-FIT SPECTRAL PARAMETERS AND 1σ ERRORS

PARAMETER	UNECLIPSED	ECLIPSED	
		Fit 1	Fit 2
n_H (10^{20} cm^{-2})	7.0(1.0)	7.0(frozen)	7.0(frozen)
α	0.94(0.02)	0.94(frozen)	0.94(frozen)
K_{pl}	$2.67(0.07) \times 10^{-2}$	$4.9(0.1) \times 10^{-4}$	$3.77(0.20) \times 10^{-4}$
E_1 (keV)	0.93(0.04)	0.93(frozen)	0.93(frozen)
σ_1	0.16(0.03)	0.16(frozen)	0.16(frozen)
K_{ga1}	$3.4(0.9) \times 10^{-3}$	6.1×10^{-5} (tied to K_{pl})	4.3×10^{-5} (tied to K_{pl})
E_2	6.0(0.1)	6.0(frozen)	6.8(0.3)
σ_2	1.0(0.2)	1.0(frozen)	2.0(0.3)
K_{ga2}	$2.2(0.8) \times 10^{-3}$	3.9×10^{-5} (tied to K_{pl})	$5.1(0.7) \times 10^{-4}$
$\chi^2/\text{d.o.f.}$	70/62	376/141	139/138
Probability	21%	$< 10^{-32}$	46%

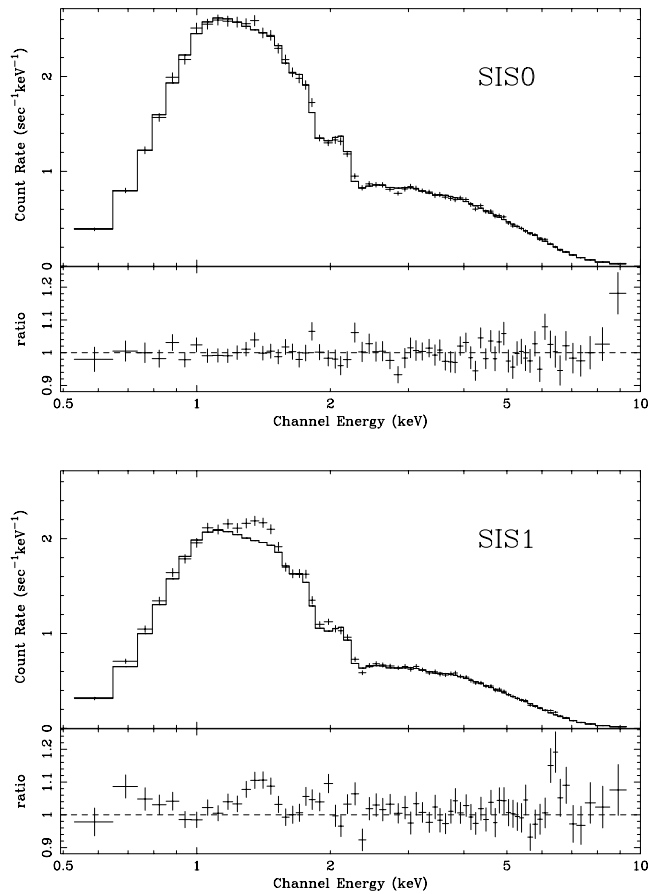


FIG. 2.—Observed spectrum of SMC X-1 out of eclipse (*crosses*) and best-fit model (*histogram*).

luminosity of 1.9×10^{38} ergs s^{-1} for a distance of 50 kpc. A source with this spectrum would give an on-axis count rate of 1.1 count s^{-1} ² in the *RXTE* All-Sky Monitor whereas the observed count rate of SMC X-1 in the All-Sky Monitor, at the peak of the high state is approximately 3 count s^{-1} (Wojdowski et al. 1998), which implies that the luminosity of SMC X-1 in its high state is approximately 5×10^{38} ergs s^{-1} .

In the eclipse observation, the systematic calibration errors are much smaller than the statistical errors due to the low count rate. Therefore, spectral models were fit simultaneously to both the SIS0 and the SIS1 detectors. To fit the spectrum derived from the observation during eclipse the same model that fit the out-of-eclipse data, scaled down in intensity, was tried. This is the spectrum that would be expected if the intrinsic spectrum of the accreting neutron star did not change between the two observations and the eclipse spectrum were due only to Compton scattering of the X-rays from the source. Relative to the rescaled out-of-eclipse spectrum, the eclipse data show a large excess at energies greater than 4 keV and a small, narrow excess near 1.8 keV, the approximate location of the fluorescence line of neutral silicon (Fig. 3). An acceptable fit for the eclipse data can be obtained by allowing the parameters of the broad

² This count rate was computed by comparing the model flux to that of the Crab (Toor & Seward 1974) in each of the 2–3, 3–5, and 5–10 keV bands and assuming that the count rate of the Crab is 25 count s^{-1} in each of these bands.

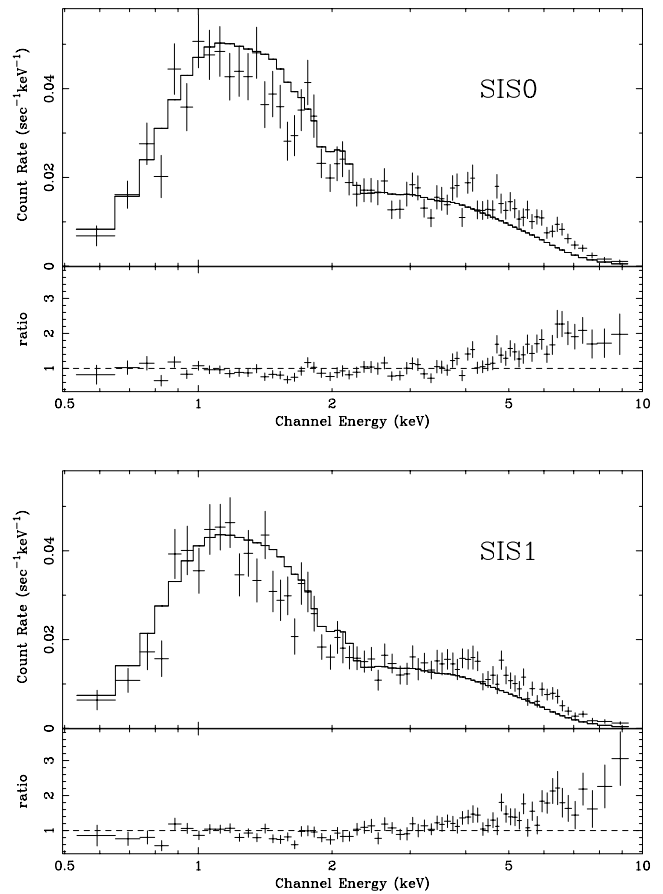


FIG. 3.—Eclipse spectrum of SMC X-1 with out-of-eclipse model spectrum.

6 keV feature to vary from their values scaled from the out-of-eclipse spectrum.

A separate fit to the data points in the 1.5–2.0 keV range was done using a power law continuum and a narrow emission feature. The energy of this emission feature was found to be 1.775 ± 0.020 keV and the flux was $1.5 \pm 0.5 \times 10^{-5}$ photon $s^{-1} \text{cm}^{-2}$. This feature is near the location of the detector's internal fluorescence peak and so we must consider the possibility that this feature is spurious. For the *AXAF* ACIS CCDs, which are similar to the *ASCA* CCDs, the probability that an X-ray with energy greater than the Si K edge will cause fluorescence in the detector is 1% just above the K edge and decreases to 0.2% at 4 keV (Prigozhin et al. 1998). The SIS0 screened event list has 4769 photons with energies above the silicon K edge, which should result in less than ~ 50 fluorescent photons produced in the detector. The measured line flux (1.5×10^{-5} photon $s^{-1} \text{cm}^{-2}$) corresponds to 74 photons in this spectrum. A miscalibration of the probability of fluorescence events of order 100% would be necessary to result in a spurious detection of this magnitude. Furthermore, in the data from the out-of-eclipse observation, in which the source has nearly the same spectrum, there is no deviation from the smooth spectral model at this energy. Also, the measured energy of this feature differs from the 1.74 keV of neutral silicon that would come from the detector but is consistent with the energy of the fluorescent line of partially ionized silicon. Still, confirmation of this feature will require better observation.

We also tried a reflection model (the “hrel” model by T. Yaqoob in XSPEC) to fit the ~ 6 keV feature—i.e., we assumed that the source spectrum could be described by a power law plus a broad ~ 0.9 keV component, and that the observed spectrum includes a component due to reflection of that spectrum from cold, neutral gas. For the out-of-eclipse spectrum, we assumed that the “escape fraction” was unity—i.e., the neutron star was directly visible. For the eclipsed spectrum we assumed the same model normalization—i.e., the neutron star had the same spectrum and luminosity as during the out-of-eclipse observation. The best-fit parameters for fits to the reflection models are given in Table 2. The out-of-eclipse spectrum requires a covering fraction that is greater than unity and therefore unphysical.

3. SPECTRAL MODELS OF REPROCESSED RADIATION

For the densities lower than approximately 10^{12} cm^{-3} , with which we are concerned, the heating, cooling, ionization, and recombination are dominated by interactions between single photons from a point source and photons and gas particles (e.g., photo-ionization) and by two-particle interactions (e.g., recombination). If the radiation from the point source is not significantly attenuated, the rate of photon-particle interactions is proportional to Ln/r^2 and the rate of two-particle interactions is proportional to n^2 . Here L is the luminosity of the point source, r is the distance from it, and n is the density of hydrogen (neutral and ionized). Spontaneous de-excitations (single particle transitions) happen on timescales short compared to the time between two-body interactions and can therefore be considered not as independent processes, but as part of the two-body interaction that produces the excited state. Therefore, for a given gas composition and a given radiation spectrum, the state of the gas is a function of the ratio of the quantities Ln/r^2 and n^2 : the ionization parameter, $\xi \equiv L/nr^2$, defined by Tarter, Tucker, & Salpeter (1969).

Reprocessed radiation includes re-emission from recombination, bremsstrahlung, and fluorescence as well as electron scattering. Bremsstrahlung and recombination radiation are two-body processes, so for a given state of the gas, their intensity is proportional to n^2 . Since, for a given gas composition and spectrum of incident radiation, the state of the gas is a function only of ξ , the volume emission coefficient for these processes may be written

$$j_v^{(1)} = f_v(\xi)n^2. \quad (4)$$

Photoionization of inner shell electron may result in a radiative cascade that fills the inner shell vacancy. Because the

resultant radiation is due to photoionization, its contribution to the volume emission coefficient is proportional to Ln/r^2 and can be written as

$$j_v^{(2)} = g_v(\xi)Ln/r^2 \quad (5)$$

$$= \xi g_v(\xi)n^2. \quad (6)$$

The contribution of electron scattering, which we consider to be an absorption followed by emission, like fluorescence, is proportional to $Ln/r^2 = \xi n^2$. Thus, for a given spectrum of primary radiation and gas composition, the entire spectrum of reprocessed emission, from given volume element dV is a function of the ionization parameter scaled by $n^2 dV$.

We used the XSTAR program v1.43 (Kallman & Krolik 1999) to calculate the spectrum of the X-rays that would be emitted by gas illuminated by radiation with the spectrum of SMC X-1. XSTAR assumes a point radiation source at the center of a spherically symmetric nebula and calculates the state of the gas and the continuum and line radiation emitted by the gas throughout the nebula. We took the spectrum of the central point source to be that derived from the out-of-eclipse observation (eq. [1]) but with the absorbing column set to zero. We set the density of the gas at a constant value of 10^{-3} cm^{-3} and did calculations for the metal abundances equal to the solar value (Anders & Grevesse 1989) and less by 0.5, 1, 1.5, and 2.0 dex. We chose a low gas density so that all optical depths would be negligible. These calculations are similar to model 1 of Kallman & McCray (1982).

While XSTAR includes some effects of electron scattering, it does not explicitly compute the “emission” owing to electron scattering. Therefore we added this component to the emissivities computed with XSTAR. Photons much lower in energy than $m_e c^2 = 511 \text{ keV}$ scatter from free electrons with little change in frequency with the Thompson cross section. Photons may also scatter from bound electrons as if the electrons were free if the binding energies are much less than the photon energies. In gases of astrophysical interest, approximately 98% of the electrons are contributed by hydrogen and helium. Since the greatest binding energy in either of these two elements is 54.4 eV, for purposes of Compton scattering of X-rays of greater than approximately 0.5 keV it is a very good approximation to assume that the electron density is a constant fraction of the hydrogen density. For the solar abundance of helium relative to hydrogen there are approximately 1.15 electrons per hydrogen atom. Thus, for X-rays in the energy range 0.5–50 keV, the spectrum of Compton-scattered radiation is identical to the spectrum of input radiation and does not depend on the ionization state or temperature of the plasma. We

TABLE 2
PARAMETERS OF REFLECTION MODEL FITS

Parameter	Uneclipsed	Eclipsed
$n_{\text{H}} (10^{20} \text{ cm}^{-2})$	8.7(0.7)	8.7(frozen)
α	1.03(0.03)	1.03(frozen)
$K_{\text{pl}} (10^{-2} \text{ ph s}^{-1} \text{ keV}^{-1} \text{ at 1 keV})$	2.81(0.06)	2.81(frozen)
σ_1 (keV)	0.16(0.02)	0.16(frozen)
$K_{\text{ga1}} (10^{-3} \text{ ph s}^{-1})$	$3.2(^{+1.0}_{-0.5})$	3.2(frozen)
Escape Fraction	1(frozen)	$1.38(0.03) \times 10^{-2}$
Covering Fraction	2.9(0.15)	0.22(0.01)
χ^2/dof	80/64	147/40
Probability	9%	33%

therefore added to the volume emissivity, the quantity

$$j_{\nu, \text{scattered}} = 1.15 \times \frac{L_{\nu}}{L} \frac{\sigma_T}{4\pi} \xi n^2. \quad (7)$$

The total spectrum of reprocessed X-rays from gas with 1/10 solar metal abundance for several ionization param-

eters is shown in Figure 4. These spectra modified by $7 \times 10^{20} \text{ cm}^{-2}$ of interstellar absorption and convolved with the *ASCA* response matrix are shown in Figure 5. In the range $1 \lesssim \log \xi \lesssim 3$, the spectrum contains many strong features from recombination to the K shells of astrophysically abundant elements. At lower values of the ionization parameter, astrophysically abundant elements are not

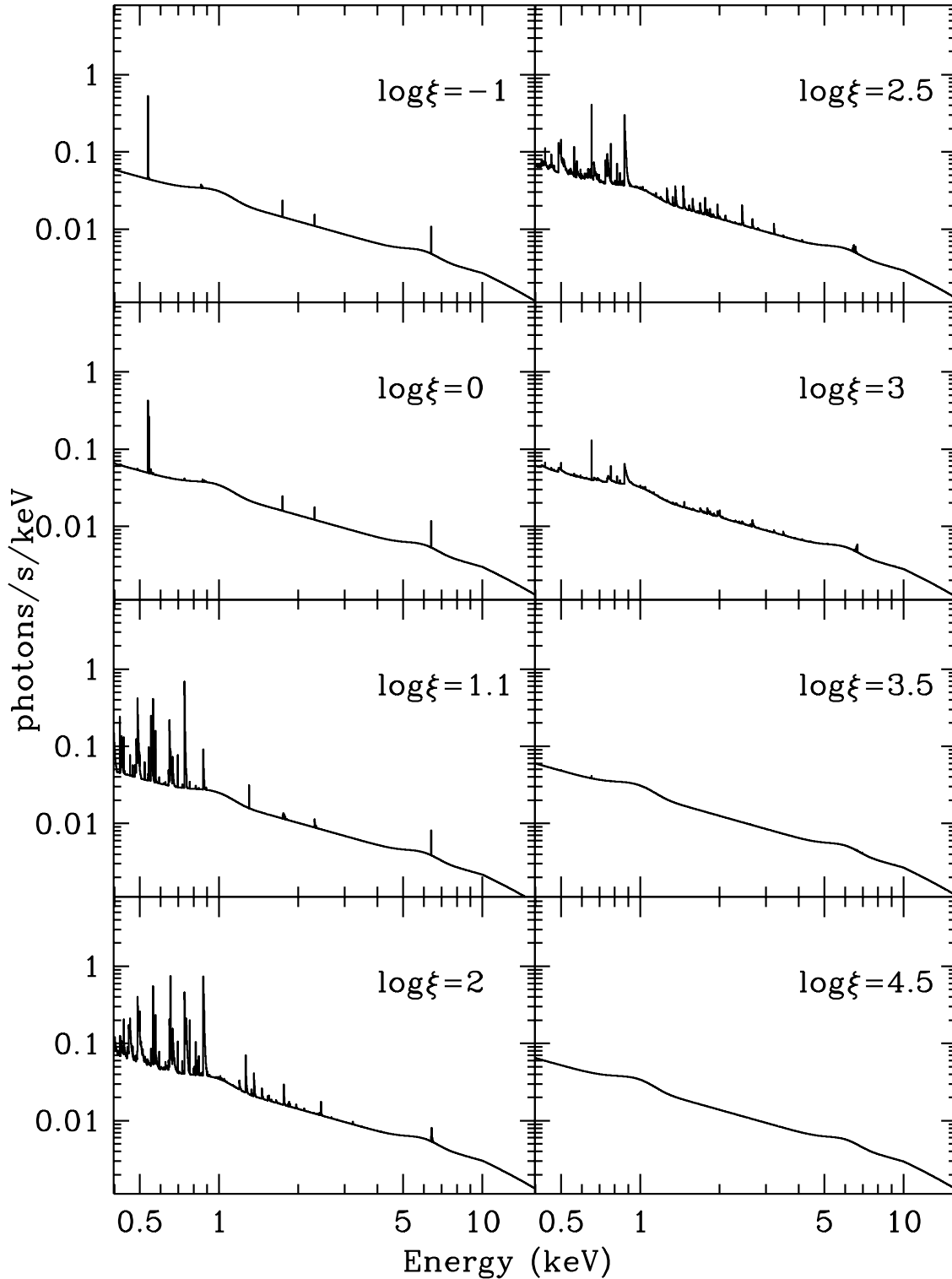


FIG. 4.—Total spectra of reprocessed (Compton-scattered, bremsstrahlung, recombination, and fluorescent) radiation for gas when illuminated by radiation of with the spectrum of the SMC X-1 out-of-eclipse model for various values of $\log \xi$. The normalizations are arbitrary and chosen such that $n^2 \xi$, which determines the magnitude of the Compton-scattered continuum, is constant between the panels. The resolution is 1340 bins per decade.

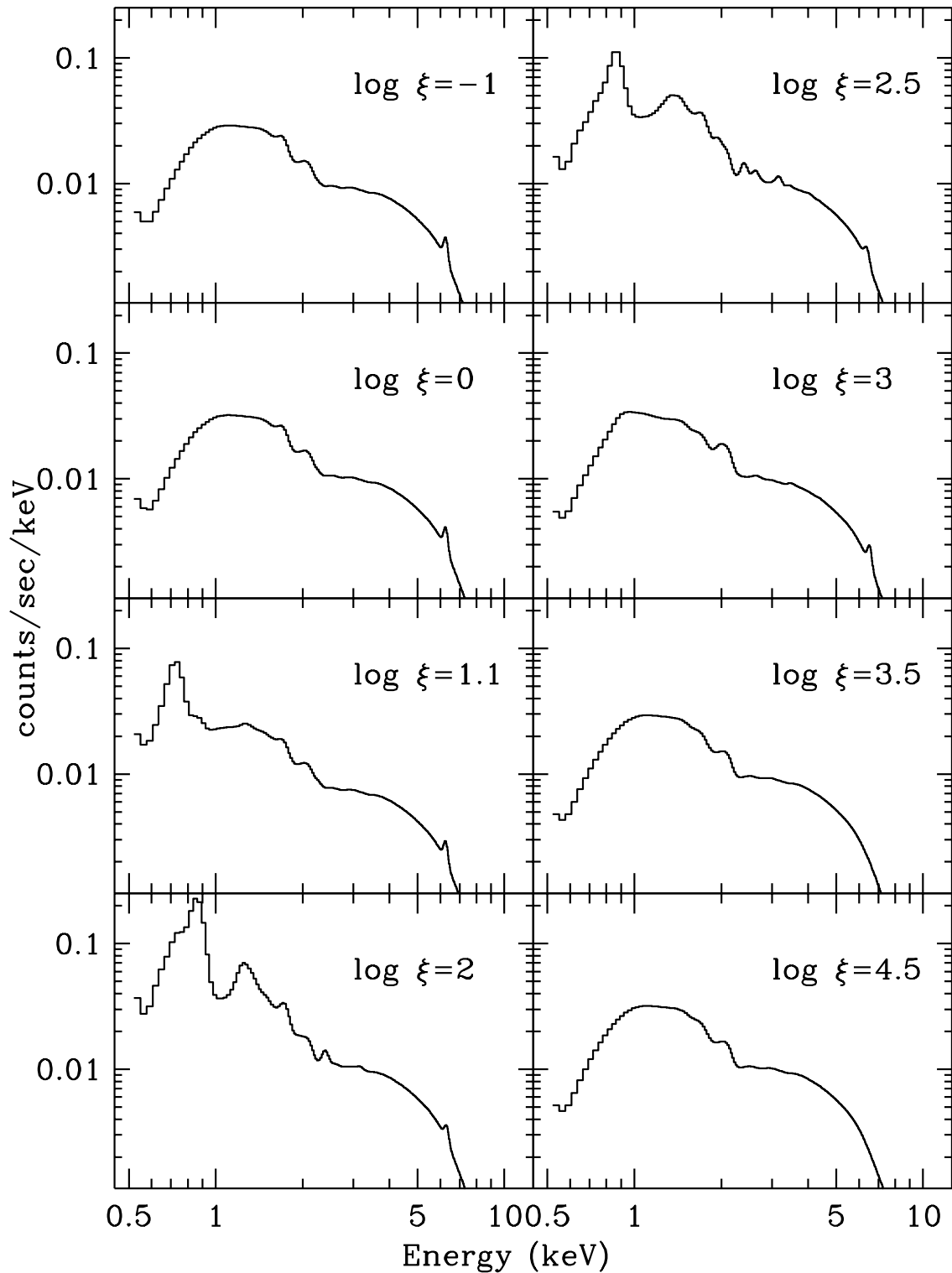


FIG. 5.—Spectra of reprocessed radiation of Fig. 4 absorbed by a column of 7×10^{20} and convolved with the *ASCA* SIS0 response

ionized up to the K shell and therefore produce spectral features in the X-ray band only by photo-ionization of K-shell electrons and subsequent radiative cascades. At higher values of the ionization parameter, the abundant elements approach complete ionization and the electron temperature approaches a limit. Therefore, the emissivity due to recombination approaches a limit while the continuum emissivity due to Compton scattering continues to

increase linearly with ξ . We have computed the cross section of photoionized material in Figure 6.

3.1. Single ξ Spectra and the *ASCA* Eclipse Spectrum

The *ASCA* spectrum of SMC X-1 in eclipse was compared to the convolved spectra of reprocessed radiation over a range of abundances and ionization parameters. None of the reprocessing mechanisms discussed above can

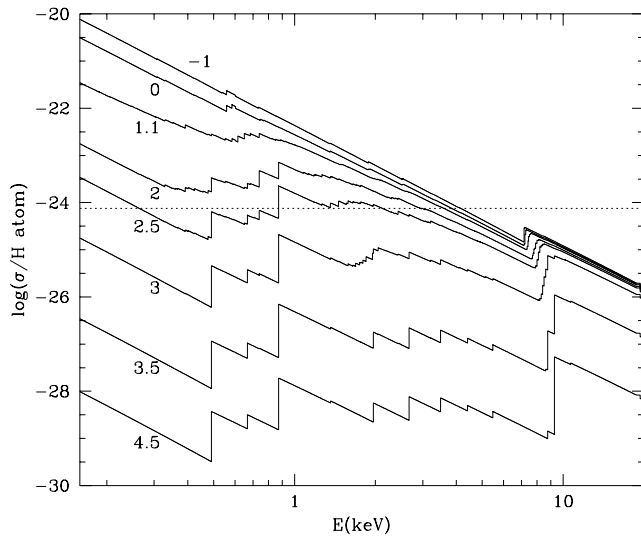


FIG. 6.—Absorption cross section per hydrogen atom for gas at various values of $\log \xi$. The dashed line is the Thompson cross section multiplied by 1.15 (the number of electrons per hydrogen atom).

reproduce the observed excess in the eclipse spectrum around 6 keV. Therefore we considered only the data for energies less than 4 keV. The eclipse spectra can be fitted by reprocessing models with $\log \xi \gtrsim 3$ or by models with $\log \xi \lesssim 1$ and metal abundance less than approximately 1/10 of solar (Fig. 7). In the range $1 < \log \xi < 3$, even for a metal abundance as low as 1/100 of solar, the calculations predict a flux below 1 keV from recombination features that is inconsistent with the observed spectrum (Fig. 8b). For $\log \xi > 3$ recombination is very weak relative to Compton scattering so the spectrum is insensitive to metal abundance and satisfactory fits may be obtained for abundance as large as solar (Fig. 8a). The fluorescent features present in the spectral models for $\log \xi < 1$ are not as strong relative to the recombination features as in the models for intermediate ionization. This allows the data to be fit with $\log \xi < 1$ as long as the metal abundance relative to solar is

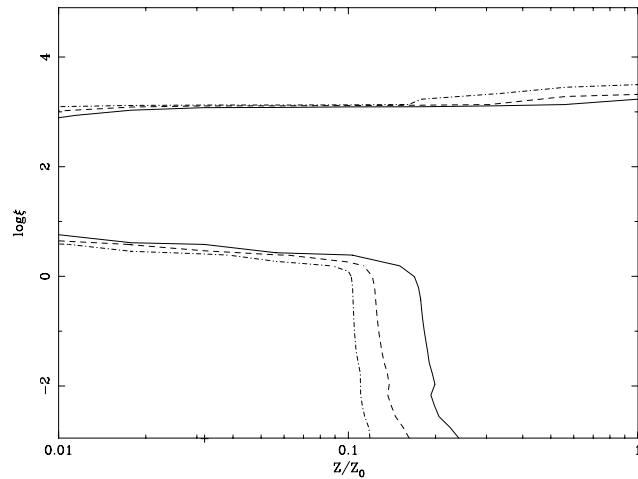


FIG. 7.—Contours of χ^2 for fits of the eclipse spectrum to reprocessing by gas at single ionization parameters and solar relative abundances. The regions of good fits are in the top and the lower left. The contours mark $\Delta\chi^2 = 2.3$ (dot-dashed line), 4.61 (dash line), and 9.21 (solid line) from the best fit (plus sign), which has $\chi^2 = 112$ with 85 degrees of freedom (dof).

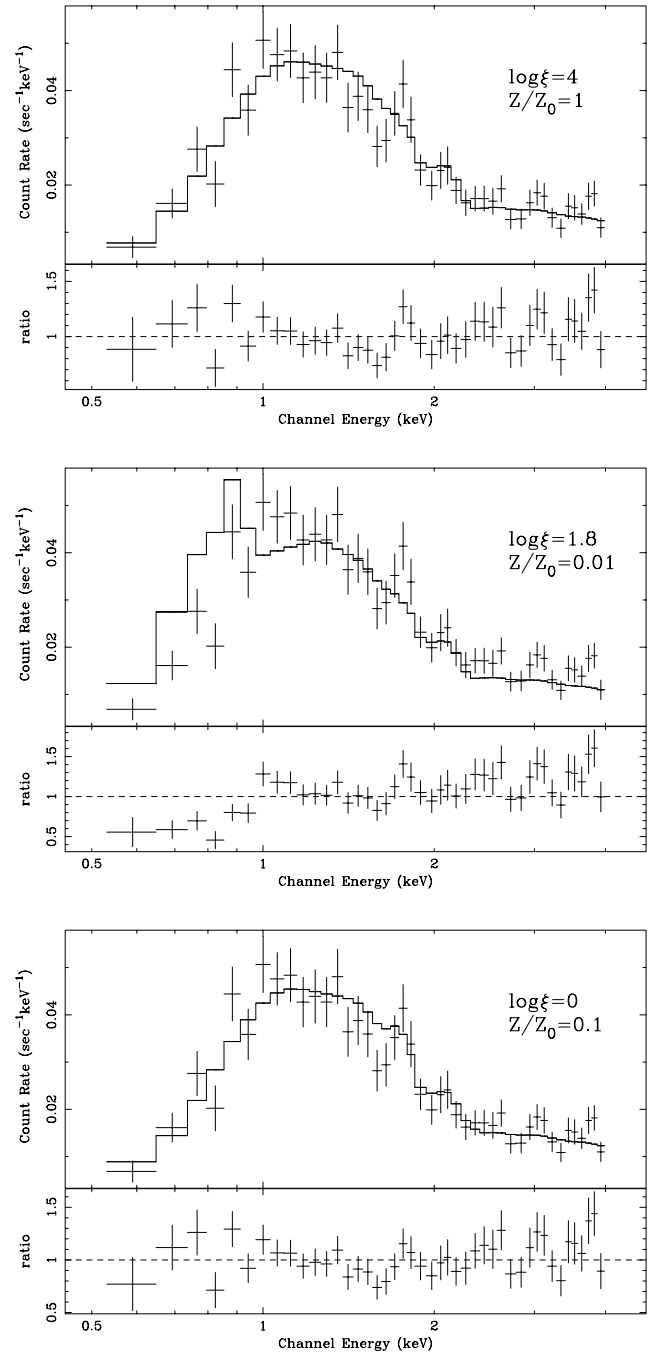


FIG. 8.—SIS0 eclipse spectrum (crosses) compared to spectra of reprocessing from gas at various single ionization parameters and solar relative abundances.

less than approximately 0.2 (Fig 8c). In contrast to the $\log \xi > 3$ regime however, the spectrum of reprocessed X-rays contains fluorescent emission lines.

The emission line detected at 1.775 ± 0.020 keV may be the fluorescent $K\alpha$ line of Si II^3 or some combination of this line and the fluorescent $K\alpha$ lines of Si III-V all of which have $K\alpha$ lines near 1.74 keV. It may also be due, at least partially,

³ We describe fluorescence lines according to the charge state of the atom at the time the line is emitted, after photoionization of the inner shell electron has occurred—e.g., K shell photo-ionization of neutral iron results in the emission of a Fe II $K\alpha$ photon.

to a higher ionization stage, such as Si IX, which has a fluorescent $K\alpha$ line at 1.77 keV. The feature cannot be due to recombination to helium-like silicon (which would produce an emission line at 1.84 keV) because under conditions necessary to produce that line, recombination radiation from oxygen and other elements would produce a large flux below 1 keV, which is not seen. The presence of this fluorescence line and the lack of strong recombination features indicate that a significant fraction of the emission comes from gas with $\log \xi < 1$. The reprocessing spectral model with $\log \xi = 0$ and metal abundance equal to one-tenth of solar has a single emission line at 1.740 keV. With the model normalization fit to the SMC X-1 eclipse spectrum, this line has a flux of 5.2×10^{-6} photon $s^{-1} cm^{-2}$. The flux of the observed feature is $1.5 \pm 0.5 \times 10^{-5}$ photon $s^{-1} cm^{-2}$. If this line flux is correct, it indicates that the silicon abundance in SMC X-1 is at least two-tenths of solar.

Except in the range $1 < \log \xi < 3$, the flux from the reprocessing models is dominated by Compton scattering. Therefore, the emission measure (n^2V) necessary to reproduce a given luminosity with a single ξ reprocessing model should be proportional to the inverse of the ionization parameter. To confirm this, the best-fit value of χ^2 was computed on a grid of values of $\log \xi$ and the normalization parameter ($K \equiv (n^2V/4\pi D^2) \times 10^{-14} cm^5$). Contours from these fits are plotted in Figure 9. Indeed, the best fits are in a narrow region of parameter space around the line defined by ($K\xi = 1.7$).

To determine what amount of material with $1 < \log \xi < 3$ is allowed by the observed spectra, fits were done to model spectra consisting of reprocessing from gas at two ionization parameters. Both components had metal abundances fixed at one tenth of solar. The first component had an ionization parameter fixed at the lowest calculated value ($\log \xi = -2.95$). The ionization parameter and the normalization of the second component were stepped through a grid of values and the normalization of the first component was varied to minimize χ^2 . Contours of the minimized $\Delta\chi^2$ relative to the best fit are plotted in Figure 10. As noted above, model spectra for $\log \xi > 3$ and for $\log \xi < 1$ have the same shape since the emission is domi-

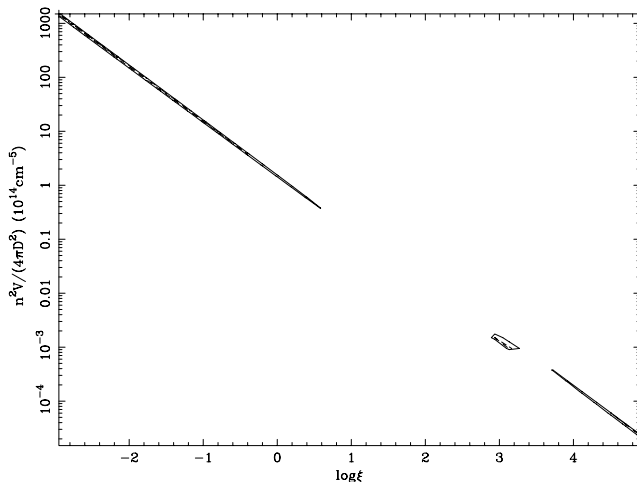


FIG. 9.—Relation between ξ and the normalization K . The solid contour marks $\Delta\chi^2 = 100$ relative to the best fit (*plus sign*).

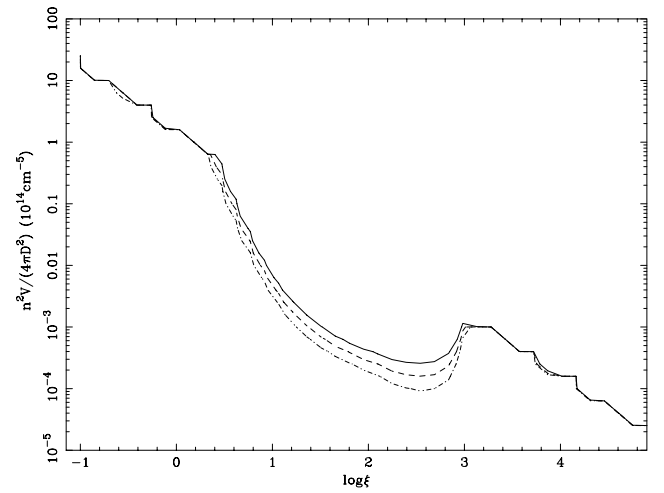


FIG. 10.—Contours of $\Delta\chi^2$ for a K and $\log \xi$ of a second component. The contours mark $\Delta\chi^2 = 2.3$ (dot-dashed line), 4.6 (dashed line), and 9.2 (solid line) relative to the best fit (*plus sign*).

nated by Compton scattering. For these values of the ionization parameter, good fits can be obtained for normalizations up to a value such that $K\xi \sim 1.7$ as above. For $1 < \log \xi < 3$ however, smaller normalizations are allowed. For $\log \xi = 2$, $K \lesssim 3 \times 10^{-4}$. For a distance of 50 kpc, this corresponds to an emission measure $n^2V \lesssim 9 \times 10^{57} cm^{-3}$.

4. SPECTRA FROM REPROCESSING IN MODEL WINDS

4.1. Spectral Simulation Algorithm

We devised a procedure to calculate the spectrum of X-rays from a central point source reprocessed in a three-dimensional matter distribution. The flux received by an observer at a distance d from a diffuse source can be written schematically as

$$\mathcal{F}_v = \frac{1}{4\pi d^2} \int j_v(x) e^{-\tau_v(x)} dV, \quad (8)$$

where x is the spatial vector, j_v is the volume emission coefficient—the energy output of the gas per unit volume, frequency, time, and solid angle in the direction of the observer. The optical depth $\tau_v(x)$ between the point of emission and the observer. The optical depth is calculated

$$\tau_v(x) = \int_x^{x_{\text{observer}}} \sigma_v(x) n(x) dx, \quad (9)$$

where σ_v is the cross section for absorption and scattering out of the line of sight per hydrogen atom. Again, we consider a photon received by the observer as having been “emitted” at the place where it last interacted with the gas.

We map the density distribution onto a rectilinear grid such that lines of sight to the observer are parallel to one of the axes. Then, for every grid cell, we calculate the ionization parameter. Then, starting at grid cells opposite the observer, we look up the spectrum of reprocessed emission for that ionization parameter, scale by n^2V , and then add that to a running total emission spectrum. At the next grid cell we attenuate the emission spectrum from cells behind

according to the cross sections for that ionization parameter scaled by nl , where l is the length of the grid cell, and so on to compute the total spectrum of emission in the direction of the observer. Emission is assumed to come only from gas that is illuminated by the point radiation source. Absorption in unilluminated material is taken to be equal to absorption from gas with the lowest ionization parameter in the XSTAR table. Emission from points of gas that are not visible to the observer (i.e., those behind the companion star) are not included in the summation.

The flux received by the observer is equal to this luminosity divided by 4π times the distance squared. The emission spectrum is thereby converted to a flux and is output to a FITS format XSPEC Table Model (Arnaud 1995), which is easily imported to the XSPEC spectral fitting program (Arnaud 1996), and can easily be convolved with instrument response matrices for comparison with observed spectral data.

Our assumption that the direct radiation from the compact object is not significantly attenuated in the gas may cause an overestimate of the radiation from circumstellar material with substantial optical depth. The cross sections plotted in Figure 6 can be as large as 10^{-21} cm² per hydrogen atom. Therefore, this algorithm will begin to fail for column densities of order 10^{21} cm⁻² or greater. The fact that this algorithm does include absorption of the reprocessed radiation on its way from the reprocessing sites to the observer does compensate for this error to some extent however. The only reprocessed radiation that will be seen from a region of large optical depth is from the part of its surface, which is both exposed to the radiation source and visible to the observer. The algorithm would not be accurate if the radiation source was surrounded by a small shell of optically thick gas. In this case, the algorithm would calculate emission from distant gas that was actually shadowed by the dense shell. However, if the optically thick material does not subtend a large solid angle about the radiation source, the error due to shadowing should be small. In regions where the density is so high that single grid cells are optically thick, the neglect of absorption by material within the same cell in which it was produced will cause the emission from those optically thick cells to be overestimated by a factor approximately equal to the optical depth of the cells. If the optically thick material subtends only a small solid angle at the radiation source and is not optically thick on length scales much less than 1 pixel, the algorithm will calculate the spectrum accurately except that the small portion of the emission that is from the dense material will be overestimated by a factor of no more than a few.

4.2. Hydrodynamic Simulation

The spectrum of reprocessed emission from the Blondin & Woo (1995) hydrodynamic simulation wind was synthesized using the algorithm described in § 4.1. The density distribution on the spherical grid from the hydrodynamic simulation was interpolated onto a rectilinear grid with similar resolution: 50 grid points along the radius of the simulation, equal to 1.43×10^{11} cm per grid point. No points in the hydrodynamic simulation had densities no larger than approximately 3×10^{11} cm⁻³ so no pixel had an optical depth significantly greater than one and the overestimate of the contribution from optically thick cell was no greater than a factor of a few. While the gas distribution

does have regions of high density near the radiation source, the high-density material subtends a small angle in the orbital plane and is mostly confined to the orbital plane so the error in the simulated spectra due to this gas should not be large. The spectral simulation was carried out for X-ray luminosities of 1, 1.7, 3, 6, 10, 17, and 30 times 10^{38} ergs s⁻¹ for metal abundances equal to solar and less by 0.5, 1.0, 1.5, and 2.0 dex. The distribution of density and ionization parameter (for $L_X = 3 \times 10^{38}$ ergs s⁻¹ for this model is shown in Figure 11.

The SMC X-1 eclipse spectrum was fit by interpolation on this grid of models. With the distance to SMC X-1 fixed at 50 kpc, reasonable fits are obtained for the luminosity in a narrow range around 6.4×10^{38} ergs s⁻¹ and for abundances less than a few hundredths of solar (Fig. 12). Though a reasonable fit to the global spectrum can be obtained (Fig. 13), the lack of a silicon line in the model spectrum indicates that the model is deficient. Furthermore, the best-fit metal abundance is very low compared to other measurements of the abundances in the SMC (Westerlund 1997). Both the reason for the low abundance and for the lack of the silicon feature can be seen in the differential emission measure, plotted in Figure 14. For an X-ray luminosity of 6×10^{38} ergs s⁻¹, the hydrodynamic simulation contains gas with $\log \xi > 3$ and also some gas with $1 < \log \xi < 3$ but no gas with $\log \xi < 1$. The presence of gas with $1 < \log \xi < 3$ produces strong recombination emission features and only by setting the metal abundances to be very low, can the calculated spectra be made to agree with observed spectrum. While the neglect in the algorithm of absorption between the X-ray source and the reprocessing point may have caused an overestimate of the recombination emission by a factor of a few, the total emission measure of material with $2 < \log \xi < 3$ in the Blondin & Woo (1995) model is 1.33×10^{59} cm⁻³ compared to the lower limit of 9×10^{57} cm⁻³ for single components with $\log \xi$ in that range derived in the previous section (Fig. 10). The lack of a silicon emission feature in the model can be explained by the absence of material at low ionization. The presence of the silicon fluorescence feature in the observed spectrum indicates that there exists gas in the wind of SMC X-1 that is more dense than any of the gas in the hydrodynamic simulations. A hydrodynamic simulation with higher spatial resolution might resolve the gas distribution into smaller, denser clumps and move the peak of the emission measure distribution below $\log \xi = 1$ where it would fluoresce but not emit recombination radiation in the ASCA band.

4.3. Absorption of the Direct Radiation

We now explore the validity of our approximation that absorption of radiation along lines of sight from the neutron star can be neglected and that the spectrum of reprocessed radiation is a function only of ξ and spectrum of the radiation from the neutron star. Examination of the Blondin & Woo (1995) density distribution—plotted in Figure 11—shows that the largest column densities occur in dense clumps. Since the densest material has the lowest ionization parameter and material at lower ionization has greater opacity, these are the places where our approximation is most likely to be invalid. The contour denoting the highest density in Figure 11 denotes a density of 10^{12} cm⁻³. The distance from the neutron star to the first clump of this density is that of 13 grid cells, which is equal to

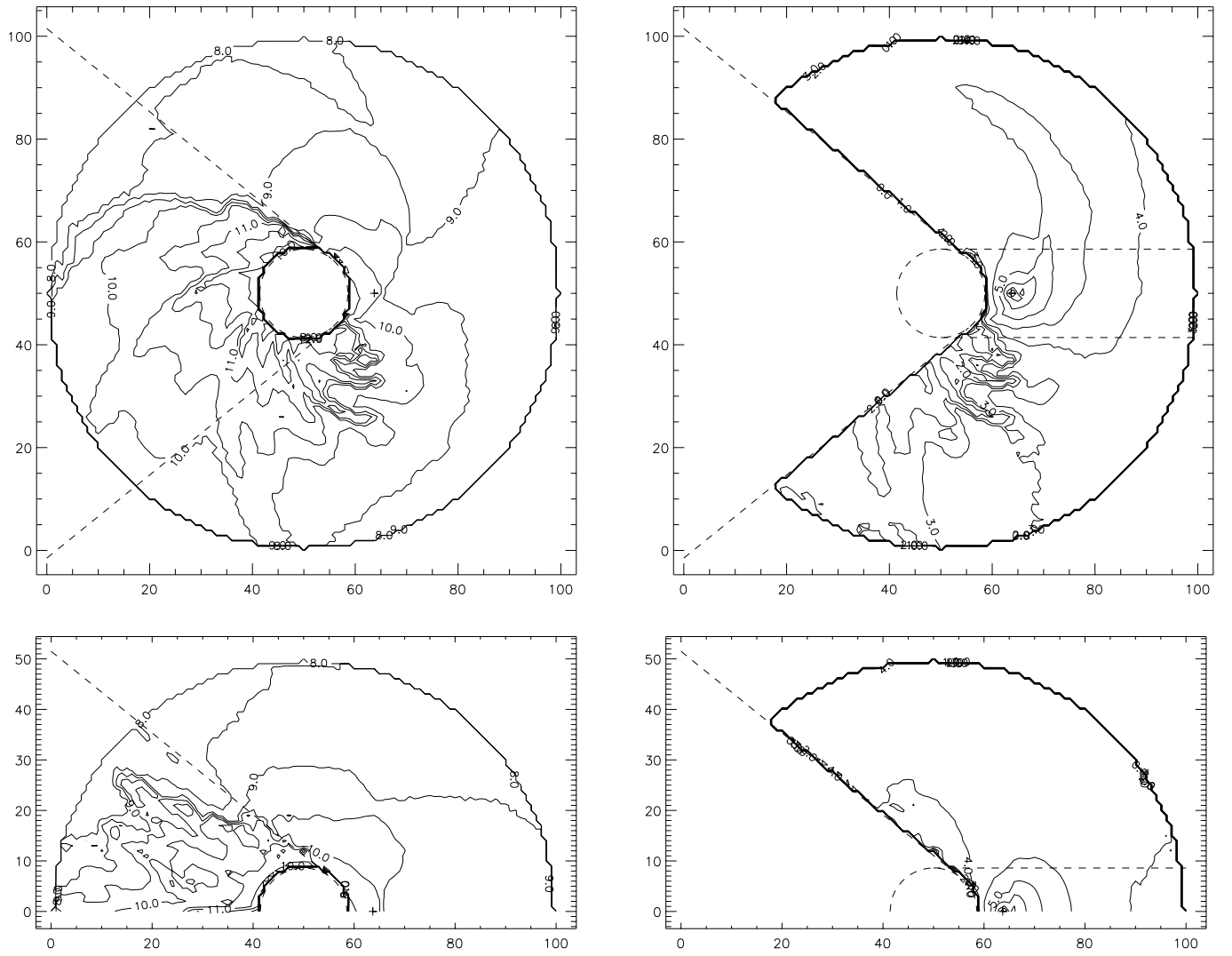


FIG. 11.—Contours of $\log n$ (left panels) and $\log \xi$ (right panels) for the hydrodynamic simulation of Blondin & Woo (1995). The top panels are the orbital plane and the bottom panels are the plane that contains the axis of rotation and the line of centers. The location of the neutron star is marked with a plus sign.

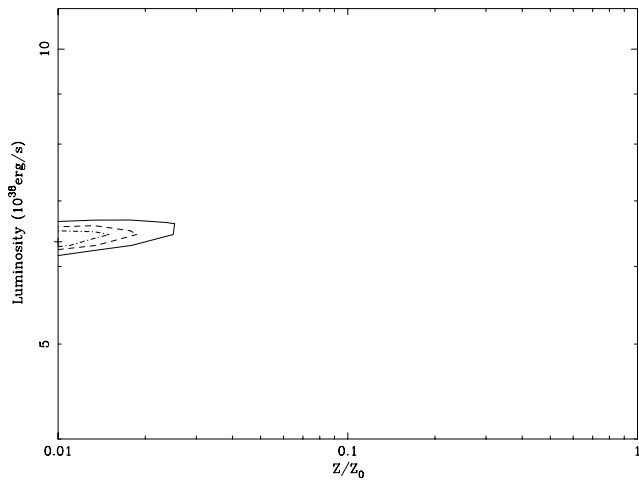


FIG. 12.—Contours of χ^2 for the spectral simulation with the Blondin & Woo (1995) matter distribution. The contours mark $\Delta\chi^2 = 2.3$ (dot-dashed line), 4.61 (dashed line), and 9.21 (solid line) from the best fit (plus sign), which has $\chi^2 = 47.5$ with 41 dof.

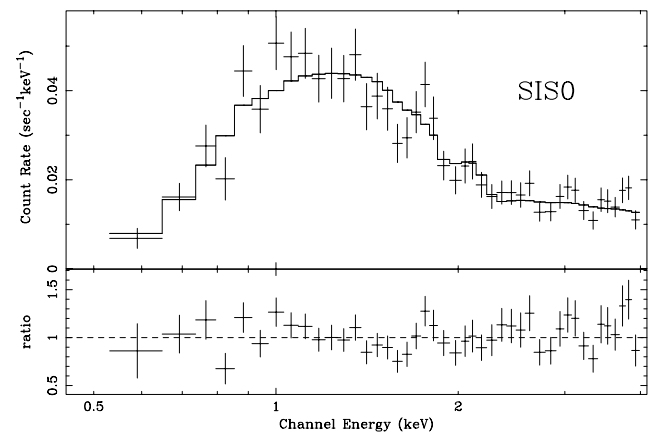


FIG. 13.—SIS0 eclipse spectrum (crosses) and best-fit synthetic spectrum for the hydrodynamic simulation (histogram, $L_X = 6.4 \times 10^{38} \text{ ergs s}^{-1}$, $Z/Z_{\odot} = 0.01$, $\chi^2 = 112$ for 86 dof).

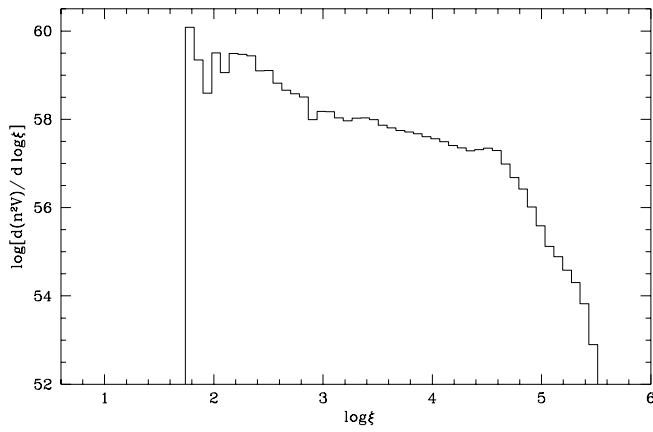


FIG. 14.—Differential emission measure of the Blondin & Woo (1995) wind distribution for $L = 6 \times 10^{38} \text{ ergs s}^{-1}$.

$1.86 \times 10^{12} \text{ cm}$, which implies $\log \xi = 2.26$. We ran XSTAR with the density equal to 10^{12} cm^{-3} , the luminosity equal to $6.4 \times 10^{38} \text{ ergs s}^{-1}$ and $\log \xi$ at the inner radius equal to 2.26. In runs with these parameters, ionization fronts like

those in the optically thick models of Kallman & McCray (1982) formed where the column depth reached approximately $2 \times 10^{23} \text{ cm}^{-2}$. In Figure 15 spectra of reprocessed radiation are shown for a point before the ionization front and after the ionization front—with the reprocessing spectral model from optically thin gas at the same ionization parameter for comparison. Before the ionization front, the spectra are almost identical for the optically thin case and the optically thick case for a given ionization parameter. After the ionization front, the spectrum of reprocessing is cut off below a few keV. Therefore, for column depths less than $2 \times 10^{23} \text{ cm}^{-2}$, absorption along the paths from the radiation source to the reprocessing sites can be ignored. Of the paths that begin at the neutron star, only those that go through the largest and densest clumps have column densities of this magnitude so the error due to the unaccounted for absorption is small.

4.4. Spherically Symmetric Winds

A spherically symmetric power-law wind distribution of the type derived by Castor et al. (1975) for a radiation-driven wind provides another model to test against the

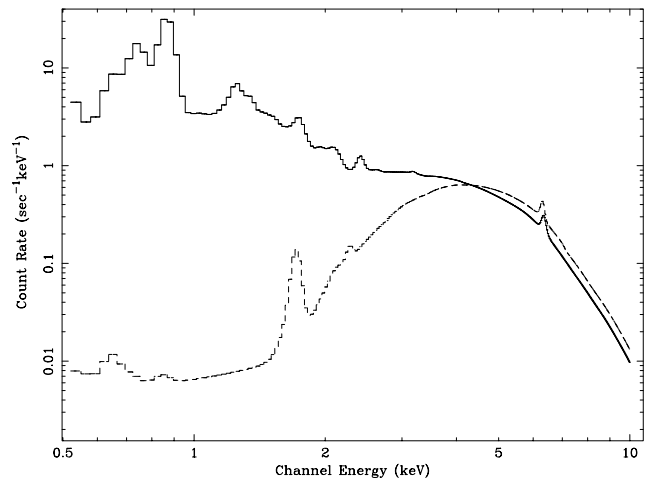
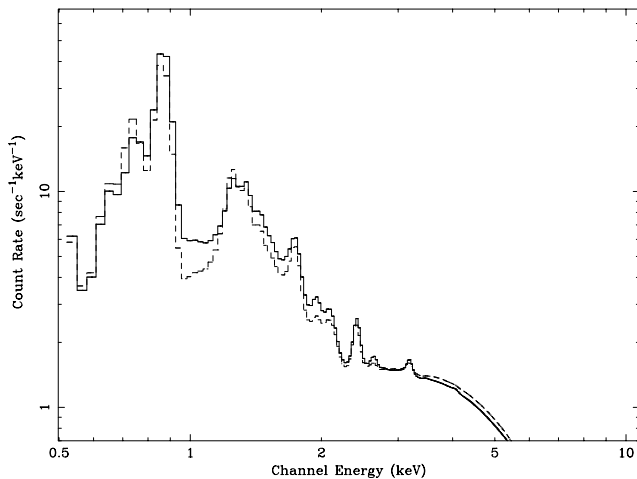
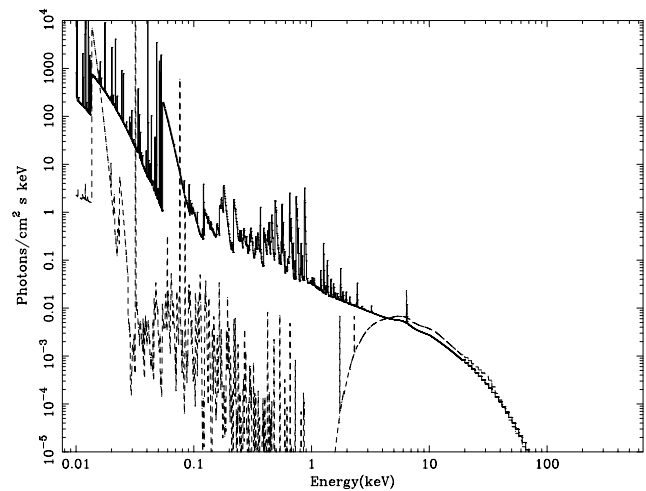
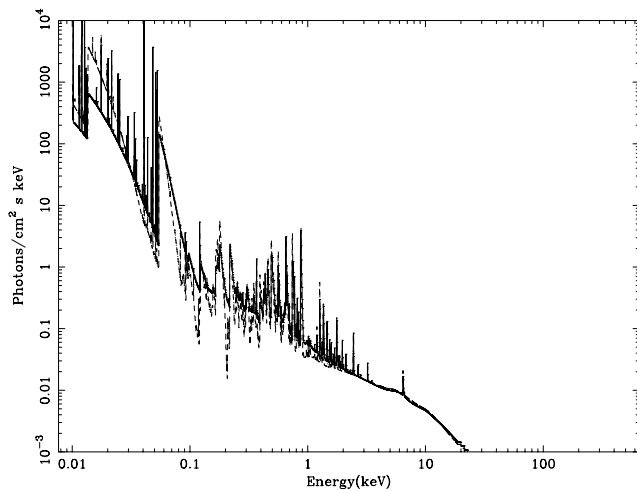


FIG. 15.—Spectra of reprocessed radiation in the optically thick case. The solid lines show the spectra of reprocessed radiation from optically thick gas. In the left panels, $\log \xi = 2.22$ and the primary radiation has traveled through 10^{23} cm^{-2} . In the right panels, $\log \xi = 1.98$ and the primary radiation has travelled through $7.15 \times 10^{23} \text{ cm}^{-2}$. The top panels show the raw spectra and the bottom panels show the spectra convolved with the ASCA response. In all panels, the dashed lines indicate the spectrum of reprocessing for the same ionization parameter in optically thin material.

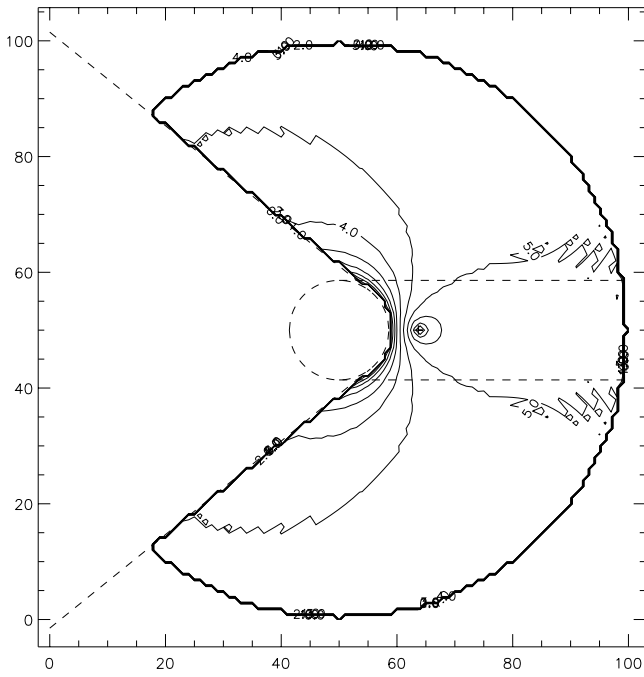


FIG. 16.—Contours of $\log \xi$ for a power-law wind plus exponential atmosphere. The ragged lines are an artifact.

observed spectrum. In this type of wind, the density is described by

$$n(r) = \frac{\dot{M}}{4\pi r^2 v_\infty \mu m_p} (1 - R_*/r)^{-\beta}, \quad (10)$$

where R_* is the radius of the star, \dot{M} is the mass loss rate, m_p is the proton mass, and μ is the mean molecular weight (the number of proton masses per hydrogen atom in the gas, ~ 1.34). In eclipse, very little of the material near the stellar surface is both illuminated by the X-ray source and visible. Therefore the expression in parentheses in equation (10) is near unity and the density is approximately proportional to r^{-2} in the region of interest. If the binary separation is not large compared to the size of the companion, then the ionization parameter does not vary far from the value it would have everywhere if the X-ray source were at the center:

$$\xi_0 = 4\pi v_\infty \mu m_p L \dot{M}^{-1}. \quad (11)$$

The density can then be written in terms of ξ_0

$$n(r) = \frac{L}{\xi_0 r^2}. \quad (12)$$

The relation $K\xi = 1.7$ derived in § 3.1 must hold approximately for $\xi = \xi_0$. In order to estimate ξ_0 , we estimate K for a spherical wind,

$$K = \frac{1}{4\pi D^2} \int n^2 dV \times 10^{-14} \quad (13)$$

and using equation (12),

$$\begin{aligned} K &= 10^{-14} (4\pi D^2)^{-1} \int_{R_*}^{\infty} n^2 dV, \\ &= 10^{-14} (4\pi D^2)^{-1} \xi_0^{-2} L^2 \int_{R_*}^{\infty} r^{-4} 4\pi r^2 dr, \\ &= 10^{-14} D^{-2} \xi_0^{-2} L^2 R_*^{-1}. \end{aligned} \quad (14)$$

Then, for $D = 50$ kpc, $L = 3 \times 10^{38}$ ergs s $^{-1}$, and $R_* = 17 R_\odot$, $K\xi_0 \approx 1.7$ implies $\xi_0 \approx 2.4 \times 10^4$ or less if only part of the flux is due to the extended wind. From equation (11) we find

$$\begin{aligned} \xi_0 &\approx 4.5 \times 10^3 \left(\frac{L}{10^{38} \text{ ergs s}^{-1}} \right) \left(\frac{\dot{M}}{10^{-6} M_\odot \text{ yr}^{-1}} \right)^{-1} \\ &\times \left(\frac{v_\infty}{10^3 \text{ km s}^{-1}} \right). \end{aligned} \quad (15)$$

So wind parameters of typical B-type stars ($10^{-7} - 10^{-6} M_\odot \text{ yr}^{-1}$, $v_t \sim 1500$ km s $^{-1}$) result a wind at high ionization and does not emit strong recombination features.

However, such a spherically symmetric high-ionization wind cannot produce the observed silicon emission feature. A component with $\log \xi < 1$ must be included. An exponential region of the atmosphere, of the type inferred from extended eclipse transitions, may be a good candidate for such a low ionization region. An atmosphere with a scale height much less than the stellar radius would be illuminated and visible in only a small region. This region has the same distance from the compact object as does the center of the companion star (1.95×10^{12} cm for SMC X-1). For this region to have $\log \xi < 1$, a density of approximately 10^{14} cm $^{-3}$ is required for an X-ray luminosity of 5×10^{38} ergs s $^{-1}$. Woo (1993) fitted *Ginga* spectra during eclipse transitions to absorption by wind models that had the form of equation (10) but with an exponential region at the base of the wind. At the minimum radius of illumination and visibility, these models have densities no greater than 5×10^{12} cm $^{-3}$. At the stellar surface these models have densities no greater than 6×10^{13} cm $^{-3}$. However, only very near eclipse transitions can material at the stellar surface be both illuminated by the X-ray source and visible to the observer. The distribution of $\log \xi$ for the best-fit parameters to one of the eclipse transitions is plotted in Figure 16 for an X-ray luminosity of 3×10^{38} ergs s $^{-1}$.

5. CONCLUSIONS

Through comparison of spectra from *ASCA* data from observations of SMC X-1 during an eclipse and archival data from outside of eclipse, we derive the following conclusions:

1. The X-ray spectrum of SMC X-1 has approximately the same form in eclipse and out of eclipse. This indicates that most of the X-ray reprocessing in the circumstellar matter is due to Compton scattering.
2. The lack of strong recombination features in the eclipse spectrum indicates that most of the gas in the wind of SMC X-1 is either highly ionized ($\log \xi > 3$) or lowly ionized ($\log \xi < 1$). Very little material is in intermediate ionization states.
3. We find evidence of a small but significant emission feature near the energy of the fluorescence line of neutral silicon (1.74 keV). The presence of this feature, if confirmed by better measurements, would indicate that a significant amount of gas must have very low ionization.
4. The Blondin & Woo (1995) model of the density distribution derived by three-dimensional hydrodynamic simulation cannot reproduce the observed eclipse spectrum. It contains a large amount of material with $1 < \log \xi < 3$, which would produce a large flux of recombination radi-

ation. The spectral resolution of *ASCA* makes these observations very sensitive to these features. However, no recombination features are detected. Also, this model does not predict any material at low enough ionization to produce the observed silicon fluorescence line. A hydrodynamic simulation with higher spatial resolution might resolve smaller, denser clumps and produce an emission measure distribution that would reproduce the observed eclipse spectrum.

5. A smooth, spherically symmetric wind could be sufficiently ionized so as not to emit recombination radiation features that would have been detectable in our obser-

vation. However, it is difficult to construct such a wind to be consistent with observation of X-ray absorption in eclipse transitions, and with the observed intensity of the silicon fluorescence line.

We thank J. Blondin and J. Woo for making available to us the density distribution from their hydrodynamic simulation in machine readable format. This work was supported in part by NASA grant NAG 5-2540. P. S. W. received support from a NASA Graduate Student Researchers Program Fellowship through Goddard Space Flight Center (NGT5-57).

REFERENCES

- Anders, E., & Grevesse, N. 1989, *Geochim. Cosmochim. Acta*, 53, 197
 Arnaud, K. A. 1995, File Format for XSPEC Table Models, Office of Guest Investigator Programs Memo OGIP/92-009, NASA Goddard Space Flight Center Laboratory for High Energy Astrophysics
 ———. 1996, in ASP Conf. Ser. 101, *Astronomical Data Analysis Software and Systems V*, ed. G. Jacoby & J. Barnes (San Francisco: ASP), 17
 Becker, R. H., Pravdo, S. H., Rothschild, R. E., Boldt, E. A., Holt, S. S., Serlemitsos, P. J., & Swank, J. H. 1978, *ApJ*, 221, 912
 Blondin, J. M. 1994, *ApJ*, 435, 756
 Blondin, J. M., Kallman, T. R., Fryxell, B. A., & Taam, R. E. 1990, *ApJ*, 356, 591
 Blondin, J. M., & Woo, J. W. 1995, *ApJ*, 445, 889
 Castor, J. I., Abbott, D. C., & Klein, R. I. 1975, *ApJ*, 195, 157
 Clark, G. W., Minato, J. R., & Mi, G. 1988, *ApJ*, 324, 974
 Clark, G. W., Woo, J. W., & Nagase, F. 1994, *ApJ*, 422, 336
 Dickey, J. M., & Lockman, F. J. 1990, *ARA&A*, 28, 215
 Ebisawa, K., Day, C. S. R., Kallman, T. R., Nagase, F., Kotani, T., Kawashima, K., Kitamoto, S., & Woo, J. W. 1996, *PASJ*, 48, 425
 Kallman, T. R., & Krolik, J. H. 1999, XSTAR v1.43, HEASARC (Greenbelt: NASA/GSFC)
 Kallman, T. R., & McCray, R. 1982, *ApJS*, 50, 263
 Kudritzki, R. P., Pauldrach, A., Puls, J., & Abbott, D. C. 1989, *A&A*, 219, 205
 Lewis, W., Rappaport, S., Levine, A., & Nagase, F. 1992, *ApJ*, 389, 665
 Liedahl, D., & Paerels, F. 1996, *ApJ*, 468, L33
 Lucy, L. B., & Solomon, P. M. 1970, *ApJ*, 159, 879
 Morrison, R., & McCammon, D. 1983, *ApJ*, 270, 119
 Morton, C. D. 1967, *ApJ*, 150, 535
 Nagase, F., Zylstra, G., Sonobe, T., Kotani, T., Inoue, H., & Woo, J. 1994, *ApJ*, 436, L1
 Orr, A., Yaqoob, T., Parmar, A. N., Piro, L., White, N. E., & Grandi, P. 1998, *A&A*, 337, 685
 Pauldrach, A., Puls, J., & Kudritzki, R. P. 1986, *A&A*, 164, 86
 Prigozhin, G. Y., Rasmussen, A., Bautz, M. W., & Ricker, G. R. 1998, *Proc. SPIE*, 3444, 267
 Sako, M., Liedahl, D. A., Kahn, S. A., & Paerels, F. 1999, *ApJ*, 525, 921
 Sato, N., et al. 1986, *PASJ*, 38, 731
 Schreier, E., Levinson, R., Gursky, H., Kellogg, E., Tananbaum, H., & Giacconi, R. 1972, *ApJ*, 172, L79
 Stahle, C. K., Ebisawa, K., Kelley, R. L., Mukai, K., & White, N. E. 1997, in *X-Ray Imaging and Spectroscopy of Cosmic Hot Plasmas*, ed. F. Makino & K. Mitsuda (Tokyo: Universal Academy), 495
 Stanimirovic, S., Staveley-Smith, L., Dickey, J. M., Sault, R. J., & Snowden, S. L. 1999, *MNRAS*, 302, 417
 Tarter, C. B., Tucker, W. H., & Salpeter, E. E. 1969, *ApJ*, 156, 943
 Toor, A., & Seward, F. D. 1974, *AJ*, 79, 995
 Westerlund, B. 1997, *The Magellanic Clouds* (Cambridge University Press)
 Wojdowski, P., Clark, G. W., Levine, A. M., Woo, J. W., & Zhang, S. N. 1998, *ApJ*, 502, 253
 Woo, J. W. 1993, Ph.D. thesis, MIT
 Woo, J. W., Clark, G. W., Blondin, J. M., Kallman, T. R., & Nagase, F. 1995, *ApJ*, 445, 896